Hindawi
Journal of Sensors
Volume 2018, Article ID 9301873, 16 pages
https://doi.org/10.1155/2018/9301873

Research Article

A Fiber Bragg Grating-Based Condition Monitoring and Early Damage Detection System for the Structural Safety of Underground Coal Mines Using the Internet of Things

Byung Wan Jo, Rana Muhammad Asad Khan, Yun Sung Lee, Jun Ho Jo, and Nadia Saleem

Department of Civil and Environmental Engineering, Hanyang University, 222 Wangsimni-ro, Seongdong-gu, Seoul 04763, Republic of Korea

Correspondence should be addressed to Rana Muhammad Asad Khan; masadkhan87@gmail.com

Received 28 July 2017; Revised 26 November 2017; Accepted 4 December 2017; Published 10 April 2018

Academic Editor: Mosbeh Kaloop

Accurate sensing is the key to structural health monitoring of underground coal mines while using fiber Bragg grating (FBG) sensors. However, the previously developed systems for structural monitoring of underground mines have been limited to monitoring without any capability of damage detection. Therefore, this study integrates a highly accurate FBG monitoring system and output-only data-driven approaches on an Internet of things (IoT)-based platform to develop a comprehensive mine structural safety system. This system relies on a Web 2.0 main server that runs data acquisition, data processing, and damage detection algorithms along with real-time information sharing at remote locations. This system was successfully implemented at the Hassan Kishore coal mine, situated in the Salt Range of Pakistan. Wavelength division multiplexing of the FBG strain sensors reliably captured the effects of dynamic and continuous coal excavation on the stability of mine roadway and access galleries. Principal component analysis, along with hierarchical clustering, was used to determine the damage indicator of the mine. The damage index was validated, showing the minimum value for 2% stiffness reduction. Thus, integration of FBG technology with the Internet can be effectively applied for early safety assessment of underground coal mines and information sharing in real time.

1. Introduction

Mining is generally considered to be a high-risk industry all over the world [1]. The ever increasing depth, complexity, and dynamicity of mining have proved themselves as challenging factors for the novel design of underground mines. In this regard, certain associated risks and hidden defaults of mine structures impose high safety threats, and seismic events are sources of mine roof stratum displacements [2]. In underground coal mines (UCMs), among the types of mine accidents (e.g., seismicity, mine support deterioration, dust explosions, and mine collapse), the most frequent cause of accidents is mine collapse [3]. For instance, in 2011, 38% of fatal accidents in UCMs in the Salt Range region, Punjab, Pakistan, were directly related to roof collapse or mine structure failure [4]. The high socioeconomic values of UCMs and risk to miners' lives make it extremely important to monitor these structures sensitively and accurately.

Nowadays, technological advancement has enabled continuous monitoring of structures with the utilization of sophisticated and accurate monitoring systems. In this regard, fiber Bragg grating (FBG) sensing has shown a wide range of applications for monitoring critical structures such as buildings, bridges, tunnels, and mines [5]. This extensive implementation of FBG sensing has occurred because of its high sustainability, high durability, long-term stability, spatial resolution, and high immunity to electromagnetism [6–9]. Recently, a Brillouin optical time domain reflectometer was successfully implemented at the El Teniente mine

in Cachapoal, Chile [10], to accurately monitor deformation in the ventilation tunnel caused by coal excavation at a nearby undercut face. Similarly, Zhao et al. [11] implemented optic fiber grating-based displacement sensors to assess the safety of underground mines. They concluded that the chances of tunnel (roadway) collapse can be minimized by efficiently monitoring mine roof displacement. Existing research [12, 13] has focused on the application of fiber optic sensors for monitoring strain, displacement, and temperature variation around underground openings. Another study [14] tested a distributed Brillouin sensing system at the laboratory scale to show the high applicability of distributed fiber optics for monitoring point-to-point deformation along the continuous length of structures with long dimensions. More detailed applications of FBG strain sensors, specifically for geotechnical studies, can be found in [15]. While previous studies have focused on the applications of FBG monitoring in complex underground structures and mines, most of these applications are limited to standard monitoring, or in some cases event reporting. Damage detection for mine structural stability and determination of a global safety index for easy and quick assessment of the mine state still need to be investigated for UCMs.

In the previous decades, rapid flourishment of the Internet of things (IoT) in various fields such as smart grids, emergency response systems, home automation, mine tailing monitoring, and mine environment monitoring has demonstrated its capabilities [16–18]. FBG monitoring combined with automatic data processing for damage detection and remote transmission can be a promising direction for enhancing the structural safety of underground mines. In this regard, already developed monitoring systems are sufficient for providing the base of the modern integrated and intelligent IoT frameworks. However, the literature lacks a system that integrates FBG-based mine structural monitoring for early damage detection and IoT-based information sharing. Therefore, this study aims at developing an accurate monitoring, analyzing damage detection, and information sharing platform to enhance structural safety in UCMs. This platform is capable of intelligently assessing mine condition by analyzing the collected data and sharing valuable information at remote places. It exploits an output-only linear data-driven approach for early damage detection in UCMs. The sensitivity of this framework is directly dependent on the compactness of clusters. In this system, data can be recalled anytime anywhere by authorized users. This system would be helpful for defining new mining laws and future designs to enhance the structural stability of UCMs. Key contributions proposed in the present study are the following:

(1) A wavelength division multiplexed (WDM) array of FBG strain sensors for underground mine condition monitoring

(2) Seamless integration of information sharing technologies, analysis tools, and models for underground mine informatics and intelligent decision making

(3) A single-valued mine damage indicator for easy and quick assessment of mine structural safety

(4) Outlier detection algorithms for damage detection of underground mines

In this study, a brief overview of FBG working principles, the adopted FBG monitoring approach, and the IoT-based integration concept for UCMs has been discussed as follows. Section 2 comments on the selection of FBG sensors for the structural monitoring of mines. Basic study models and algorithms for damage detection are summarized in Section 3. The implemented case study followed by the results and discussions are explained in Sections 4 and 5.

1.1. Basic Principle of the FBG-Based Monitoring System. Various FBG techniques, methods, and instruments have been introduced and utilized in the past. Specifically in structural health monitoring (SHM), well-known techniques of fiber optics include optical time domain reflectometer (OTDR), Raman optical time domain reflectometer (R-OTDR), Brillouin optical time domain reflectometer (BOTDR), Surveillance d'Ouvrages par Fiber Optiques (SOFO), extrinsic Fabry-Perot interferometers, and FBG sensing. Despite being expensive and sensitive to fiber bending, FBG sensing has always been highly regarded and extensively used for SHM. This can be attributed to its simple demodulation, high multiplexing, water and corrosion resistance, and utilization in both localized and quasi-distributed networks, which enable high suitability for SHM in severe and harsh conditions [19, 20].

The perceiving units of FBG sensing are designed to pass light of a certain wavelength, while reflecting any other wavelength from the grating; thus, each sensor has its own wavelength [21]. In FBGs, external temperature and strain changes have a strong influence on shift change in wavelengths [20, 22]. The basic principle of the FBG sensor technique is shown in Figure 1. Usually, strain measurements are highly affected by temperature variations; therefore, there should be temperature compensation for strain measurements. In this regard, there are two approaches for temperature compensation, either installation of an FBG temperature sensor in close vicinity of the FBG strain sensors, or use of a tight fiber with tight contact to the monitoring structure and another loose separate fiber for temperature monitoring [15]. The simplest case for counteracting the intrinsic temperature effect induced in an FBG strain sensor is to install an external FBG temperature sensor. The temperature-induced shift wavelength can be compensated by the following [22].

$$\frac{\Delta\lambda_B}{\lambda_B} = \left[\frac{1}{n}\zeta + \alpha_f\right]\Delta T + (1 - P_e)\Delta\varepsilon. \quad (1)$$

Here, $\Delta\lambda_B/\lambda_B$ is the ratio of the displacement wavelength to the Bragg's wavelength, n is the reflective index of the fiber core, ΔT is the temperature increment, and $\Delta\varepsilon$ is the strain increment. ζ, α_f, and P_e are the thermos-optical coefficient of the fiber, thermal expansion coefficient of the fiber, and

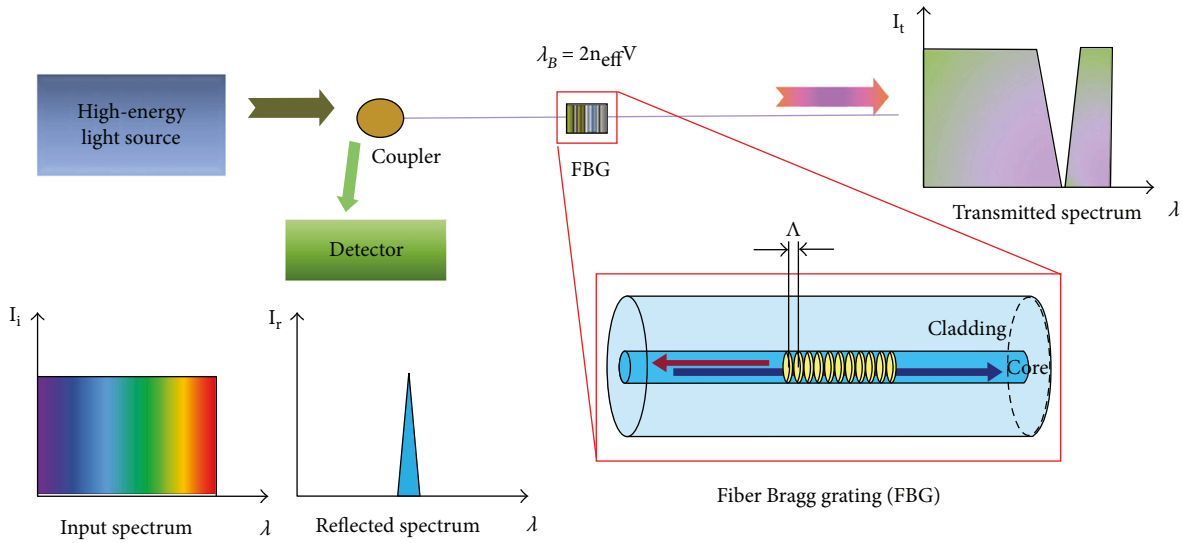

Figure 1: Schematic of basic principle of a fiber Bragg grating monitoring system.

effective elasto-optical coefficient, respectively. These coefficients are

$$\xi = \left(\frac{1}{n}\right)\left(\frac{dn}{dT}\right),$$
$$\alpha_f = \left(\frac{1}{\Lambda}\right)\left(\frac{d\Lambda}{dT}\right), \quad (2)$$
$$P_e = \left(\frac{1}{n}\right)\left(\frac{dn}{d\varepsilon}\right),$$

where Λ is the grating period and ε is the axial strain. In the case of a normal fiber, the shift change of the central reflected Bragg wavelength follows the relation

$$\Delta\lambda_B = \lambda_B(\alpha + \zeta)\Delta T. \quad (3)$$

Therefore, (1) becomes

$$\varepsilon = \frac{(\Delta\lambda/\lambda_B - \Delta\lambda_B/\lambda)}{(1 - P_e)}. \quad (4)$$

1.2. IoT System Concept. The IoT architecture for structural mine safety is shown in Figure 2. Usually, IoT architecture is comprised of three layers: the perception layer, perceiving layer, and application layer. The *perception layer* enables detection, collection, and recognition of events occurring in the surroundings of an object. This layer requires hardware network development to attain complete information of the structure, for example, sensor nodes and actuators. In this study, FBG strain and temperature sensors along with an interrogator are the basic data collection and monitoring elements. The *perceiving layer* is the convergence of theory and technology; therefore, this layer was designed with statistical models and analytical tools to detect any abnormality in the collected datasets of the underground mine. For information transmission, this system utilizes a real-time database (RODB) and a constrained application protocol (CoAP) based on extraction transform and load (ETL) technique and online analytical processing (OLAP). The *application layer* is always highly regarded in the architecture of IoT services and enables remote information sharing. In this study, a Web 2.0 page-based main server that follows OGC SWE standards [23] and enables real-time data analysis and remote information sharing was used as the base station to forecast any dangerous conditions and allow necessary measures to be taken.

2. Materials

2.1. FBG Sensors. A complete network of FBG monitoring is comprised of FBG sensors, signal transmission, data acquisition, and a data processing unit. Sensor selection is highly dependent on the monitoring requirements and environment. Despite the widespread use of embedded FBG strain sensors, they have limitations such as (i) the entry point of embedded sensors can be easily damaged and is prone to breakage, (ii) the optical fiber can be pressed, and (iii) during installation of the embedded FBG sensors, the surrounding strain field can be disturbed because of distortion of the surrounding material [24]. In the present case, drilling a hole for installation of the embedded FBG sensors would alter the stress field in its surroundings or possibly badly damage the mine roof strata because of weak geology. Therefore, this study utilized nonembedded FBG strain sensors to monitor the behavior of the surrounding rocks in response to excavation. We used 50 cm OS3610 (Micron Optics, NE Atlanta, GA, USA) (Figure 3(b)), as it has shown high compatibility with harsh environments, is cost-effective, can be used alone or in an array, and measures the average strain over the gauge length [25]. OS3610 has a strain limit of 5000 $\mu\varepsilon$ with a standard wavelength of 1512–1586 nm in a temperature range of −40°C to 80°C. As strain measurements are highly affected by temperature variations, an FBG temperature sensor for temperature compensation was also used. The nominal temperature of the surrounding rocks was less than 40°C, which is covered by the measuring range (−40°C to

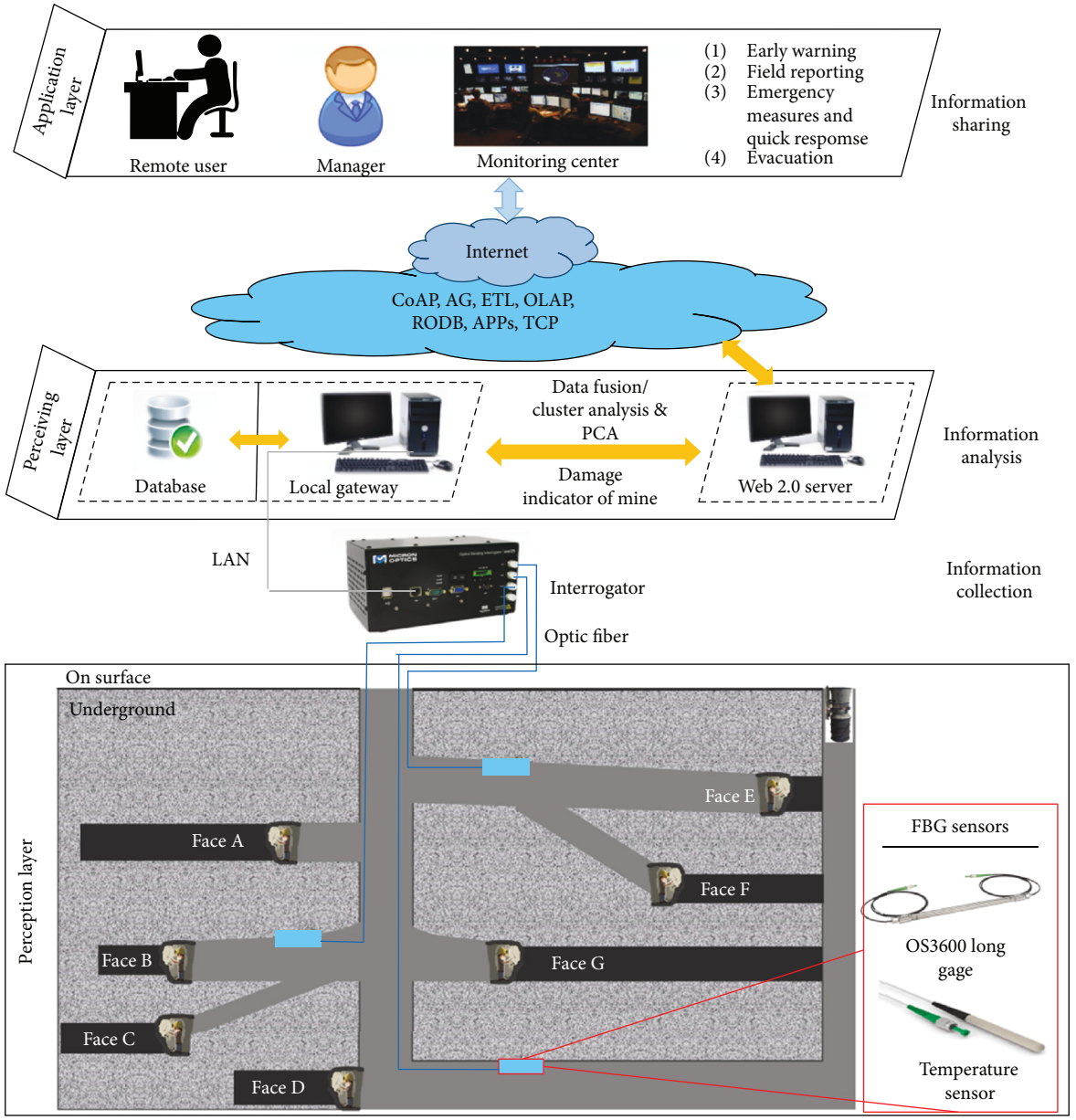

Figure 2: Architecture of the proposed IoT system for the structural safety of underground mines.

120°C) of the OS4300 FBG temperature sensor (Figure 3(a)). Moreover, this sensor has high sensitivity and high accuracy [26]. The difference between the FBG sensors and the temperature can be determined by separately evaluating the Bragg wavelength shifts for both FBGs $(\Delta\lambda_{B,1}, \Delta\lambda_{B,2})$ with their respective strain and temperature sensitivities (k_ε, k_T) [27, 28].

$$\begin{bmatrix} \Delta\lambda_{B,1} \\ \Delta\lambda_{B,2} \end{bmatrix} = \begin{bmatrix} K_s & KT_{B,1} \\ 0 & KT_{B,2} \end{bmatrix} \begin{bmatrix} \Delta\varepsilon \\ \Delta T \end{bmatrix}. \quad (5)$$

Signal transmission and data acquisition frequency were set to 1.0 Hz. In order to minimize attenuation losses due to bending and long distance, the transmission medium of acrylate-coated SMF-28 fiber with a resolution of 0.25 ± 0.05 nm and an effective bending radius of 25 mm was used. This optical fiber has been widely adopted for communication and meets ITU-T recommendations G.652 and TIA/EIA-492CAAA; more specific details can be found in [29]. An SM125-500 interrogator designed by MOI (Optics Micron Inc.), highly suitable for long-term monitoring, was used as the data acquisition device (Figure 3(c)). The SM125-500 has a four-channel Fabry-Perot tunable filter and displays the full spectrum in the working wavelength range of 1510–1590 nm [30]. The scan frequency is 2 Hz with a dynamic range of 50 dB (Table 1). The entire framework was managed through a PC server (AMD Phenom (TM)) II ×4945 Processor 3.00 GHz with 8 G RAM

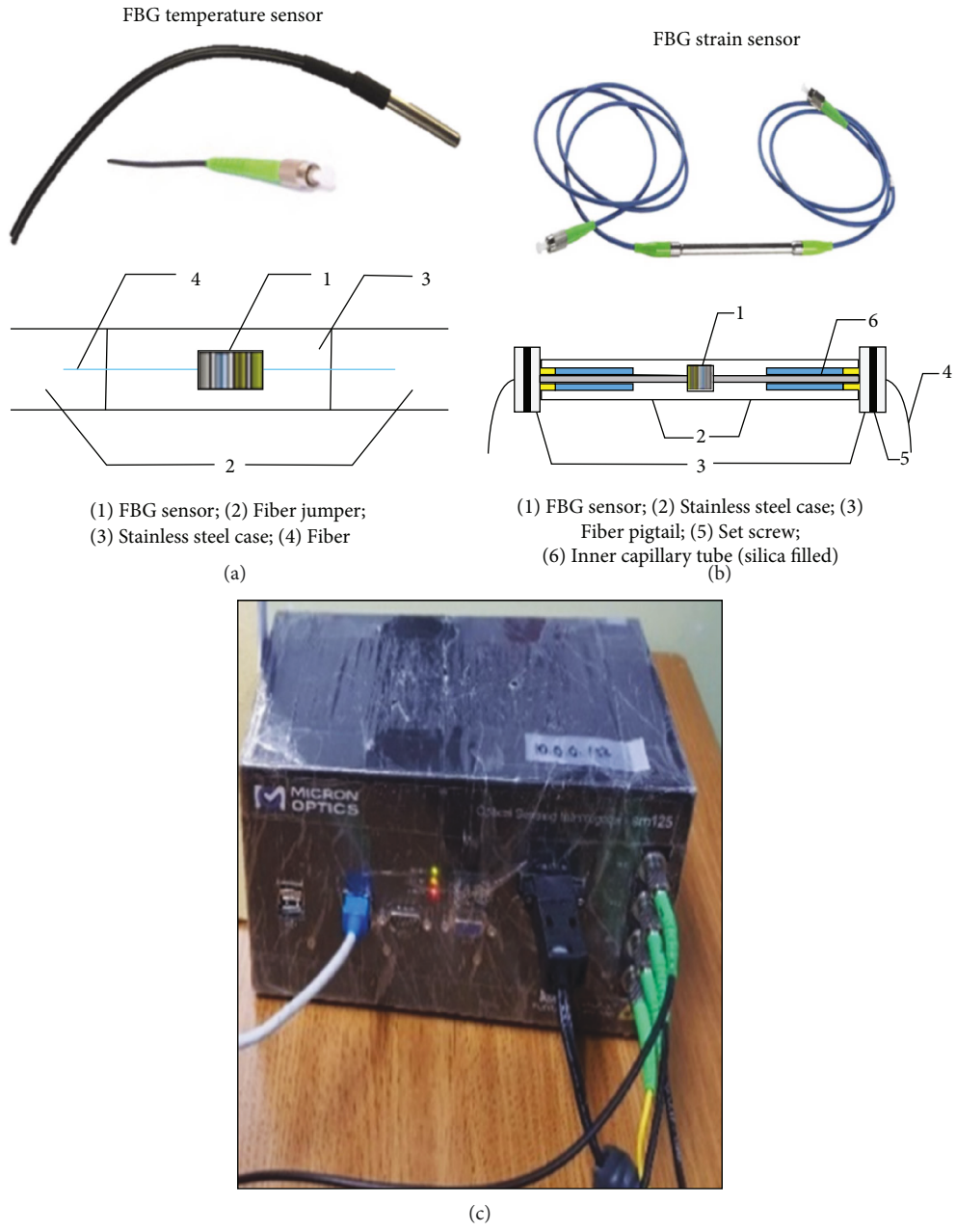

Figure 3: (a) FBG temperature sensor and schematic, (b) FBG strain sensor and schematic, and (c) SM125-500 interrogator.

and the Windows 7 operating system (Microsoft, Redmond, WA, USA).

2.2. Calibration. In this study, FBG strain sensor calibration was done with a bare FBG. The bare FBG sensor and encapsulated sensor were attached to the opposite ends of a steel coupon. Epoxy resin was used as the adhesive material for the bare FBG while cyanoacrylate was used as the bonding agent for the FBG strain gauge. Finally, the steel coupon was placed in a universal testing machine to note the variations of $\Delta\lambda_B$ and ε under the applied forces. Figure 4(a) shows the linear relationship between $\Delta\lambda_B$ and ε with a strain sensitivity of 1.2 pm/$\mu\varepsilon$. Without considering any effects of temperature and strain, this relationship can be expressed as

$$\lambda_B = 0.0012x + 1554.4. \quad (6)$$

Three FBG temperature sensors with different central wavelengths and a mercury thermometer with 0.05°C accuracy were selected. A standard bath method was implemented for determination of the temperature sensitivity coefficient of the FBG strain sensors. Each FBG sensor was placed separately in a bathtub for temperatures of 10, 15, and 20°C with increments of 1°C. The linearity constant between $\Delta\lambda_B$ and

Table 1: Specifications of SM125-500 interrogator [30].

Specifications	SM125-500
Number of optical channels	4
Scan frequency	2 Hz
Wavelength range	1510–1590 nm
Wavelength scalability; accuracy	1; 1 pm
Dynamic range	50 dB
FBG sensor capacity	60–120
Full spectrum measurements	Yes
Repeatability	0.5 pm at full speed and 0.2 pm with 10 averages
Optical connector type	FC/APC
Operating temperature range	0 to 50°C
Operating humidity	95%
Power consumption at 112 VDC	20

ΔT was found to be 0.99 with a temperature sensitivity of 5.1 pm/°C, shown in Figure 4(b) and given by

$$\lambda_B = 0.0519x + 1546.8. \tag{7}$$

3. Study Models

3.1. Strategy for Action Distinction. In general, there are two approaches for damage detection in SHM: (i) the inverse (input-output) approach and (ii) the forward (input-only) approach. The inverse approach defines models and updates these models, while the forward approach extracts valuable information directly from the input data (monitored data) without acknowledging any prior models. In recent years, forward approaches have attracted global attention from researchers because of their simplicity and advanced data analytics [31, 32]. Among the forward approaches, the most prevalent techniques are those that combine data from different sensors without losing important information. Such approaches include principal component analysis (PCA) [33], time-frequency analysis [34], and autoregressive models [35]. PCA is a powerful tool for data reduction of high-dimensional datasets without losing important information. Moreover, it implicitly counts the effects of different processes without considering them [36, 37]. Critical applications such as UCMs, where life risks are involved, demand efficient and sensitive monitoring systems with simple data analysis techniques so that any structural changes or destability can be timely reported. Therefore, the present study utilized a PCA-based normalization approach for efficiently reducing the large datasets obtained during UCM monitoring.

The dissimilarity of scales and magnitudes in the monitoring parameters is a common aspect in SHM. Therefore, it is of prime importance to process the collected raw data before application of any statistical tool. In this regard, the present study implemented autoscaling on the raw data as the initial step for damage detection. Autoscaling has shown high suitability for systems with variables of different units [38] and is given as

$$\bar{x}_{ijk} = \frac{x_{ijk} - \mu_{jk}}{\sqrt{\sigma_{jk}^2}}. \tag{8}$$

From the scaled data, consider, if "m" is the number of installed FBG strain sensors and n is a set of response measurements, then $\mathbf{X}^{n\times m}$ is the entire dataset. Usually, PCA is comprised of linear mapping of original coordinate system ($\mathbf{X}^{n\times m}$), and a new set of principal component (PCs) variables is $\mathbf{Y}^{m\times n}$ and is given by

$$\mathbf{Y}^{m\times n} = \mathbf{U}^{m\times m}\left(\mathbf{X}^{n\times m}\right)^T. \tag{9}$$

The orthogonal linear transformation matrix $\mathbf{U}^{m\times m}$ is a result of the eigenvalue problem solution of the correlation matrix $\mathbf{C}^{m\times m}$ of the original data $\mathbf{X}^{n\times m}$ given by

$$\mathbf{C}^{m\times m}\mathbf{U}^{m\times m} = \Delta^{m\times m}\mathbf{U}^{m\times m}, \tag{10}$$

where Δ is a diagonal matrix consisting of the positive or null eigenvalues from the correlation matrix $\mathbf{C}^{m\times m}$. For sensitive and precise monitoring, an important and complicated phase of PCA is the selection of the optimal number of PCs. This study uses the broken stick (BS) rule to identify the optimal numbers of PCs. This rule enables damage feature extraction at the global scale and distinguishes between normal and abnormal readings. For damage detection in SHM, the variation in eigenvectors should be significant. However, limited availability of abnormal data relative to the entire dataset makes eigenvector variation insignificant. Therefore, a moving window of constant width should be defined that covers the entire range of appropriate numbers of PCs. PCA should be performed on each defined window, and the final results should be combined, resulting in a matrix of PCs from various moving windows. The generated matrix should be divided into training and monitoring phases, and sensitivity analysis should be performed on this matrix for easy feature extraction using the BS rule. The BS rule evaluates the randomness of each PC and extracts meaningful PCs. The propagation of eigenvalues using the BS rule for the k^{th} components is given by

$$b_k = b(p, k) = \left(\frac{1}{P}\right)\sum_{i=k}^{P}\left(\frac{1}{i}\right), \tag{11}$$

where p is the total principal component and BS follows the rule; if the value of eigenvalue of the k^{th} component is greater than b_K then it is considered from the domain of global damages. This proposed forward approach applies PCA and the BS rule in sequence and extracts the datasets of uncorrelated variables. The selection of optimal PCs reflects early damage and hereby is useful for damage detection.

3.2. Damage Detection Scheme. The basic aim of damage detection is to identify any damage before its occurrence. An essential stage of damage detection is outlier detection, which relies on distance measurements. Recently, specifically for SHM, various approaches have been adopted for the distance measurement during damage detection and quantification [39]. The present study uses symbolic datasets, as these are less voluminous, less specific, compact, and more

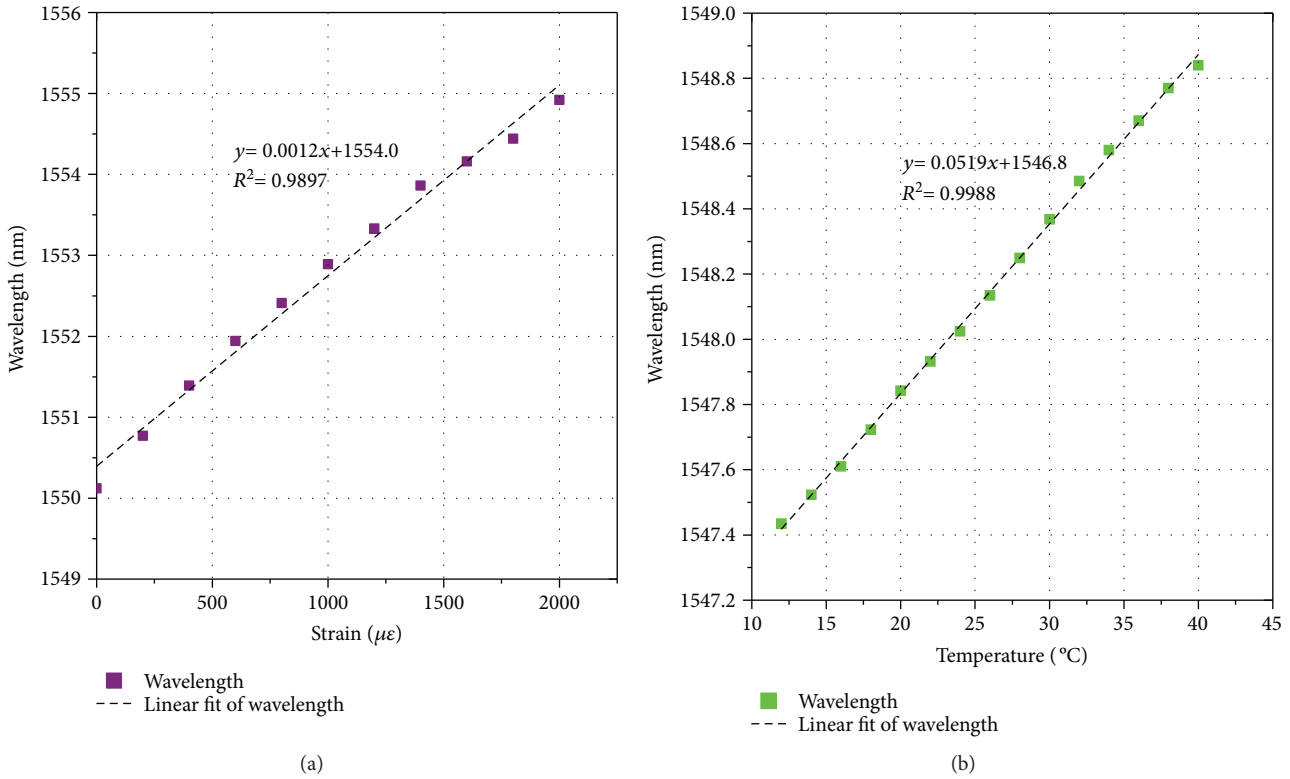

Figure 4: Calibration results of FBG (a) strain and (b) temperature sensors.

sensitive relative to classical datasets. Such symbolic datasets are based on symbolic distance measurements [40]. Symbolic distances of objects were determined using the normalized Euclidean Ichino-Yaguchi distance, as they have high sensitivity to early damage detection in SHM [41]. For two symbolic objects O_a and O_b from the dataset for $s = 1, \ldots, N$, the interquartile intervals are $O^{(r)}{}_{a,\inf}$ and $O^{(r)}{}_{a,\sup}$ and $O^{(r)}{}_{b,\inf}$ and $O^{(r)}{}_{b,\sup}$, and the normalized Euclidean Ichino-Yaguchi distance measure $d_{ab} = d(O_a, O_b)$ is given as

$$d_{ab} = \sqrt{\left(\frac{1}{P}\sum_{r=1}^{P}\frac{1}{|Y_r|}\left[\varphi_r(T_a, T_b)\right]^2\right)}, \tag{12}$$

where

$$\varphi_r(O_a, O_b) = \left|O_a{}^{(r)} + O_b{}^{(r)}\right| - \left|O_a{}^{(r)} \times O_b{}^{(r)}\right| + \gamma\left(2\left|O_a{}^{(r)} \times O_b{}^{(r)}\right| - \left|O_a{}^{(r)}\right| - \left|O_b{}^{(r)}\right|\right), \tag{13}$$

γ is a predefined constant ranging from 0 to 0.5, and $|Yr|$ is given by

$$|Y_r| = \left|\max_s\left[T^{(r)}_{\sup}\right] - \min_s\left[T^{(r)}_{\inf}\right]\right|. \tag{14}$$

These symbolic distances obtained from PC clustering are highly compact yet distinguishable in groups and subsets. Clustering minimizes the distances within a cluster and maximizes the intercluster distances. Hierarchical cluster analysis is a well-known approach for damage detection in SHM [42]. Moreover, hierarchical clustering requires fewer monitoring stations and fewer samples compared to other clustering approaches. More details on hierarchical statistical analysis for damage detection in SHM can be found in [43]. The present study implements hierarchical clustering for data fusion and data compaction, establishing a correlation between damages and structural states. In this regard, the hierarchical dendrogram contains significant information related to early damage detection; it merges a pair of clusters based on their distances and defines a new higher level. The formation of new higher levels continues until a single cluster is obtained. Consequently, hierarchical cluster analysis defines the fusion of monitoring datasets. Within a cluster dataset containing k clusters $P_k = [C_1, \ldots, C_k]$, the distance $W(P_k)$ is

$$W(P_k) = \frac{1}{2}\sum_{k=1}^{k}\sum_{c(a)=k}\sum_{c(b)=k} d_{ab}. \tag{15}$$

$C_{(i)}$ is the allocation rule for element i in cluster k and is dependent on d_{ab}. If N is the total number of objects in the cluster, the intracluster dissimilarity is

$$T = \frac{1}{2}\sum_{a=1}^{N}\sum_{b=1}^{N} d_{ab}. \tag{16}$$

In order to update clusters and achieve cluster convergence, it is viable to determine the relative heights between

clusters instead of directly using classified clusters. This study uses the relative distance D between clusters by considering one cluster as the reference cluster. The use of a dendrogram makes it easy to determine D for all clusters. In damage detection, cluster distances from the reference cluster are normalized as [0, 1]. Distances greater than or equal to 1 represent the healthy state while values between 0 and 1 correspond to the damaged state. Any damages enlarge the dissimilarity between healthy and damaged states of the structure, resulting in a decrease of D. Usually, in cluster analysis, the smallest cluster contains each measurement and the biggest cluster comprises all measurements. Figure 5 describes a flowchart scheme for damage detection for the present study.

3.3. Single-Valued Damage Index of Mine. The single-valued damage sensitive indicator of a mine from arbitrary numbers of sensors and their measurements is dependent on accurate determination of the cluster level in the entire dataset and finding the distance between clusters. This indicator is named the damage indicator of the mine (DIM), which is highly correlated with early damages by considering the responses of all sensors. The mathematical formulation of DIM is

$$\mathrm{DIM}(r) = \frac{d_{ab}^{D}(r) - d_{ab}^{H}}{\max\left(d_{ab}^{D}(r) - d_{ab}^{H}\right)}, \tag{17}$$

where d^D is the structural damaged state, d^H represents the healthy state, and r is the rth measurement. In order to compare damages, DIM must be dimensionless while being proportional to the damages. Here, DIM varies between 0 and 1, with 0 indicating a healthy state and 1 indicating a damaged state of the structure. In this study, DIM was compared with Mahalanobis distance in a vector form. This approach was inspired by [44], which expressed an alternative form of the damage indicator as

$$\begin{aligned}\mathrm{DIM}_m(r) &= 1 - \mathrm{MAC}\left(\bar{d}_{ab}^{D}(r), \bar{d}_{ab}^{H}\right) \\ &= 1 - \frac{\left(\left(\bar{d}_{ab}^{D}(r)\right)^{T}\left(\bar{d}_{ab}^{H}\right)\right)^{2}}{\left(\left(\bar{d}_{ab}^{D}(r)\right)^{T}\left(\bar{d}_{ab}^{H}(r)\right)\right)\left(\left(\bar{d}_{ab}^{H}\right)^{T}\left(\bar{d}_{ab}^{H}\right)\right)}.\end{aligned} \tag{18}$$

Similar to DIM, DIM_m varies between 0 and 1, with 1 representing a damaged state and 0 corresponding to a healthy state. Another comparison of the proposed damage indicator is to compare it with a conventional index calculated from the Euclidean distance between the vectors of two objects obtained from PCA. This index corresponds to a pattern $\underline{\mathbf{c}} = c_i$, $i = 1,2,\ldots,N$, defined as Euclidean distance between the pattern $\underline{\mathbf{c}}$ and the result of it to the network $\underline{\hat{\mathbf{c}}}$.

$$z = \left\| \underline{c} - \underline{c_i} \right\|, \tag{19}$$

where $\underline{\mathbf{c}}$ is compressed by PCA, i is the ith measurement, and z is the mean distance between the ith component of $\underline{\mathbf{c_i}}$ and the original $\underline{\mathbf{c}}$. The normalized form can be expressed as

$$N(z) = \frac{z - \min(z)}{\max(z) - \min(z)}. \tag{20}$$

This value also varies between 0 and 1, with 0 indicating a healthy state and 1 indicating a damaged state.

4. Case Study

4.1. Site Description. The IoT system developed was tested at the underground Hassan Kishore mine situated 48 km southeast of Kallar Kahar nearby Ara Basharat in the eastern Salt Range of Punjab province, Pakistan (Table 2). The coal seam in this particular area is located at an average depth of 79 m with a thickness of 0.1–0.5 m. The main roadway of this mine is connected to coal excavation galleries. A round shaft and a rectangular inclined entry connect the underground working faces to aboveground. Typically, for roadways (1.8×2.12 m) and longwall sections of an underground mine, rock support consists of wooden stacks filled with excavated shale. High overburden, deep excavation and constantly changing stresses because of mining activity are major causes of mine roof deformation, imposing a great threat to the safety of miners. Therefore, to enhance safety, it is necessary to monitor rock behavior as a response to the continuous excavation process. Moreover, other advantages of rock monitoring include reduction in the operation costs of mines and future design considerations.

The entire network of the proposed system is shown in Figure 6. In an underground opening, deformation is usually high at the center of the opening. Therefore, the main monitoring concern was strain measurements at the axial center of mine openings. Cross section widths of the mine openings were the deciding factor for length determination of the FBG array. The sensing array behaves in a similar manner as an elastic beam with two fixed ends and transverse loading when attached to the mine roof. Thus, it measures tensile strain; as long as there is no loading, the wavelength of each grating remains constant and changes with loading variations.

4.2. Sensor Array and Installation. In order to select the most appropriate locations for FBG sensor installation, site engineers and geological maps of the mine openings were comprehensively consulted. This consultation pointed out four different critical sections due to their associated weak geology and high probability of roof collapse (Figure 6). Thus, it was necessary to monitor the effects of continuous coal excavation on these weak areas. Each critical section was equipped with an array of FBG sensors. Typical installation points in all sections were on the roof of the mine opening. Each array was comprised of an FBG temperature sensor for temperature compensation and two FBG strain sensors. Each sensor had a different wavelength. The array had three aluminum segments (Figures 7(b) and 7(c)) of 500 mm length, two for the FBG strain sensors, and one for the temperature sensor. The strain and temperature sensors were multiplexed using

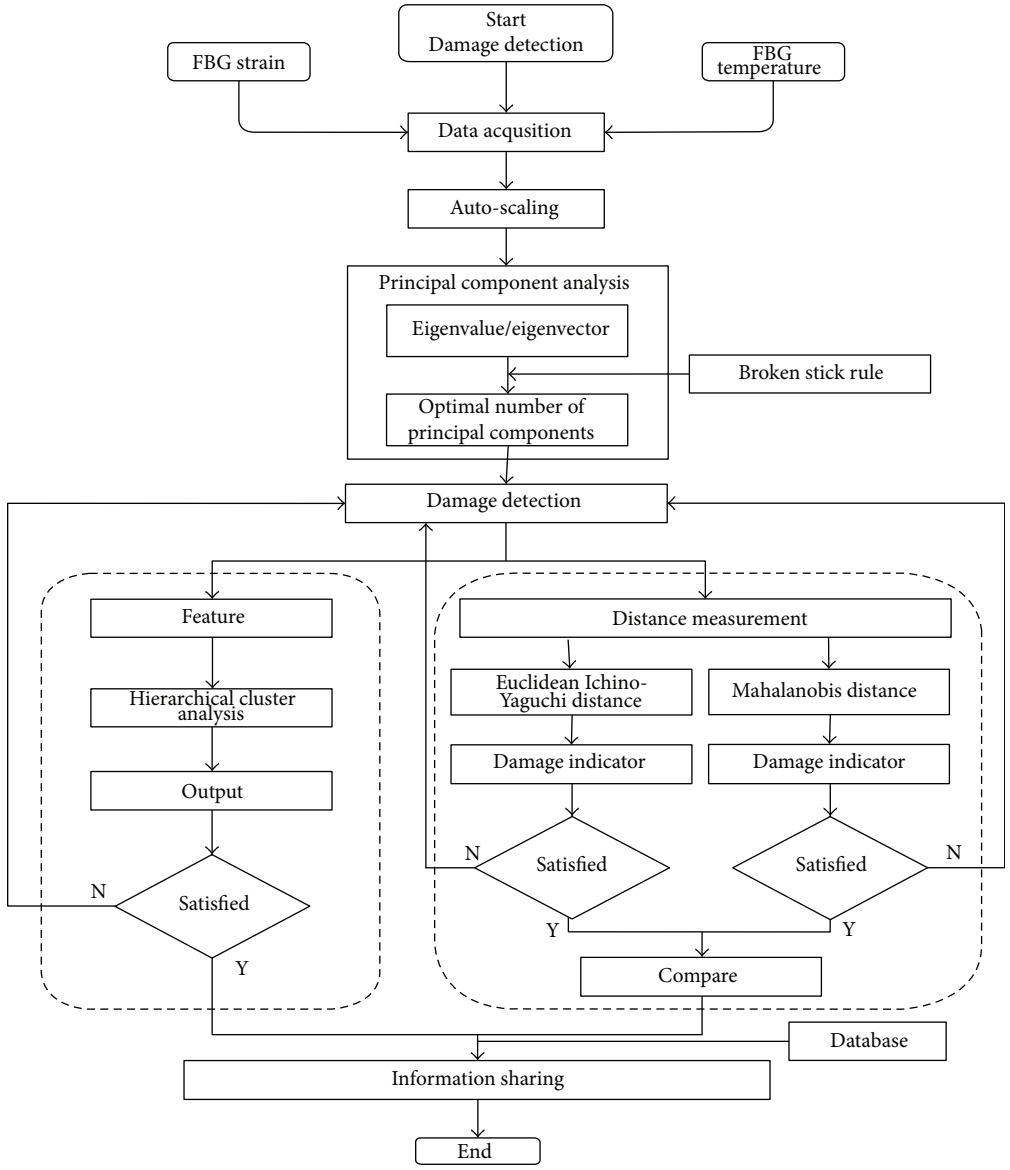

Figure 5: Flowchart of the damage detection strategy for the structural safety of mines.

Table 2: Location and elevation of the Hassan Kishore mine.

Longitude	Latitude	Elevation
32° 46′ 26″ N	73° 06′ 45″ E	870 M

a WDM technique. Suitable packing should be provided to the bare FBG sensors as they are very fragile and delight in nature. Therefore, the sensors were encapsulated and glued inside an aluminum segment. The FB grating length for each segment was 10 mm. The connection between the sensors attached to the aluminum segments was ensured using couplers for undamaged Bragg wavelength transmission. Each array was designed to fully deflect mine roof deformation. The FBG strain sensors were capable of measuring ±2500 $\mu\varepsilon$, as either tensional or compressional strain. The resolution of the FB grating was highly dependent on the capability of the attached interrogator. In this case, the resolution of the SM125-500 interrogator was 1 pm, which is equivalent to 1 $\mu\varepsilon$ (strain) and 0.1°C (temperature).

Rock surfaces are usually uneven and rough; therefore, it was necessary to prepare the surface for smooth and uneven applications of FBG sensors. In the present study, the rock surface of the mine roof was conditioned, cleaned, then abraded by silicon carbide papers (320 grit and 400 or finer) to remove uneven surfaces. Filling was applied to seal the rock surface and to fill pours. Afterwards, FBG sensor layouts were drawn and marked. The area was properly cleaned and previously fabricated FBG sensor arrays were attached to the cleaned surface using M-bond GA-2. Attachment of the FBG sensor arrays was in the transverse direction of the mine opening axis (Figure 7(a)). In addition to primary bonding, steel clamps and screws were also used to support and ensure firm anchorage of the array in case the bonding failed. Eight

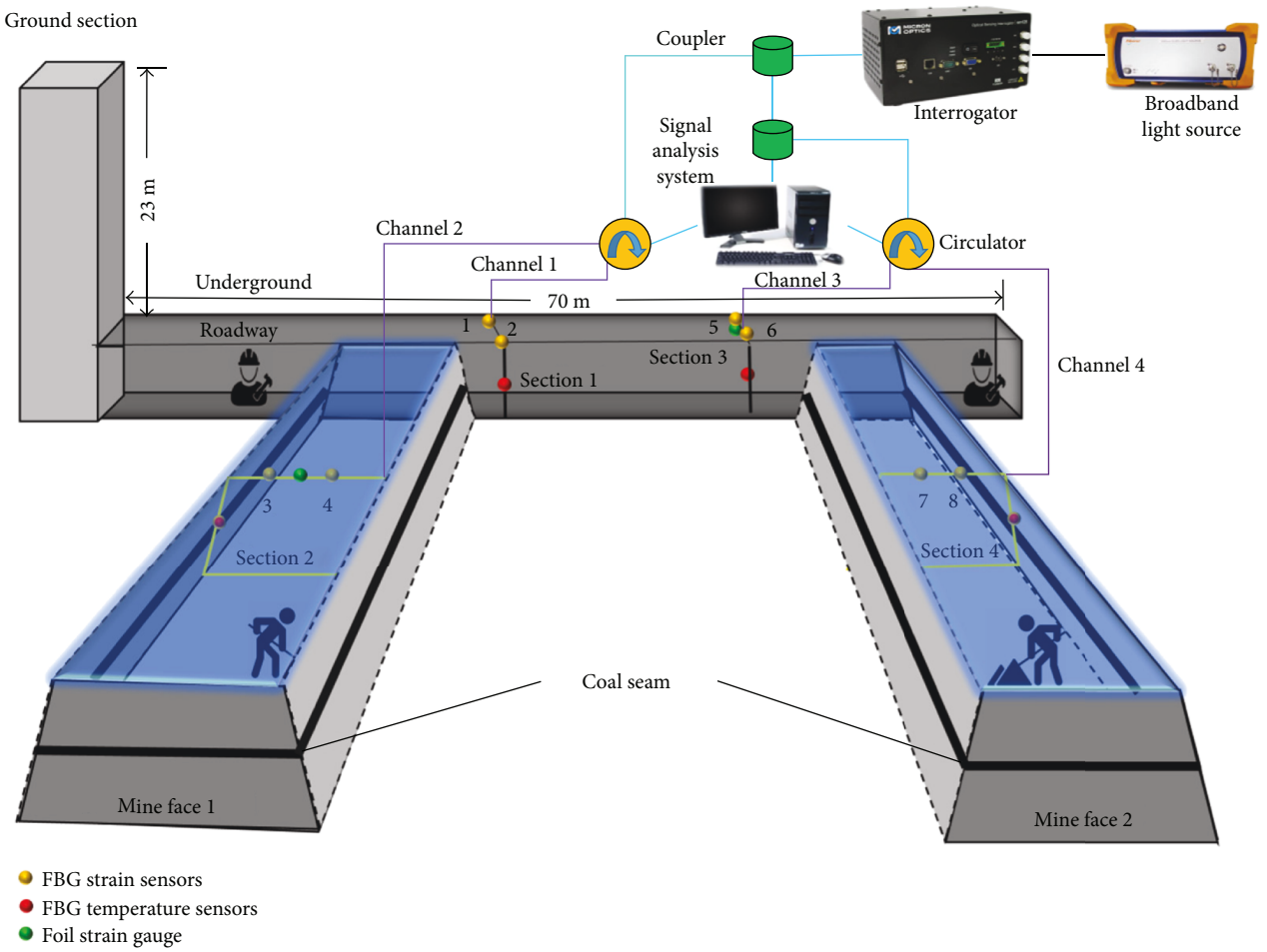

Figure 6: FBG monitoring network scheme of the Hassan Kishore mine.

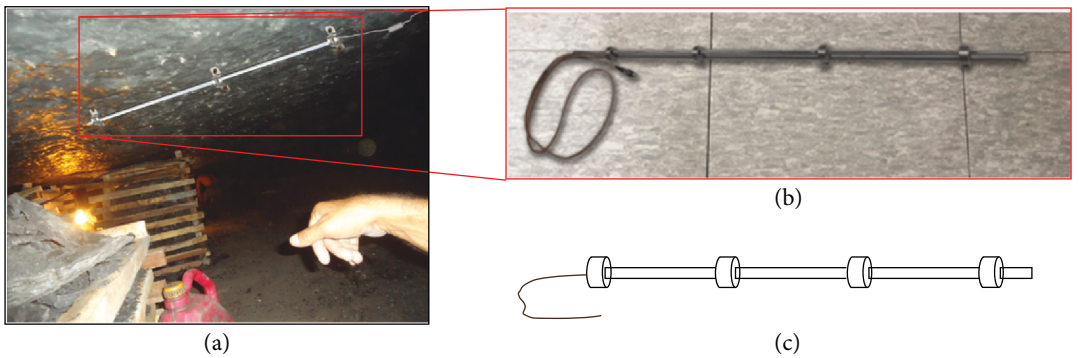

Figure 7: (a) FBG arrays attached to the mine roof. (b) Visual aspect of the FBG strain sensor array. (c) Schematic of the FBG strain sensor arrays.

screws were used to fix each array. Along the FBG array, the position of these screws and clamps was located at the couplers. Steel clamps were fitted firmly so that the array casing and clamps made an integral whole unit. The fiber coming out of each array was also protected to ensure it remained undamaged.

After complete installation and tightening of the FBG sensors, the first step was to validate the readings from the FBG strain sensors to define the healthy state baseline. Therefore, a foil strain gauge (YFLA-5) was attached to the outer surface of aluminum pipe of each FBG arrays installed at sections 2 and 3. The cross plot of strain monitoring results against time (10 days) for both FBG and foil gauge approaches is shown in Figure 8 (zoomed portions). The monitoring results from both approaches were found in good agreement with each other. After the completion of initial

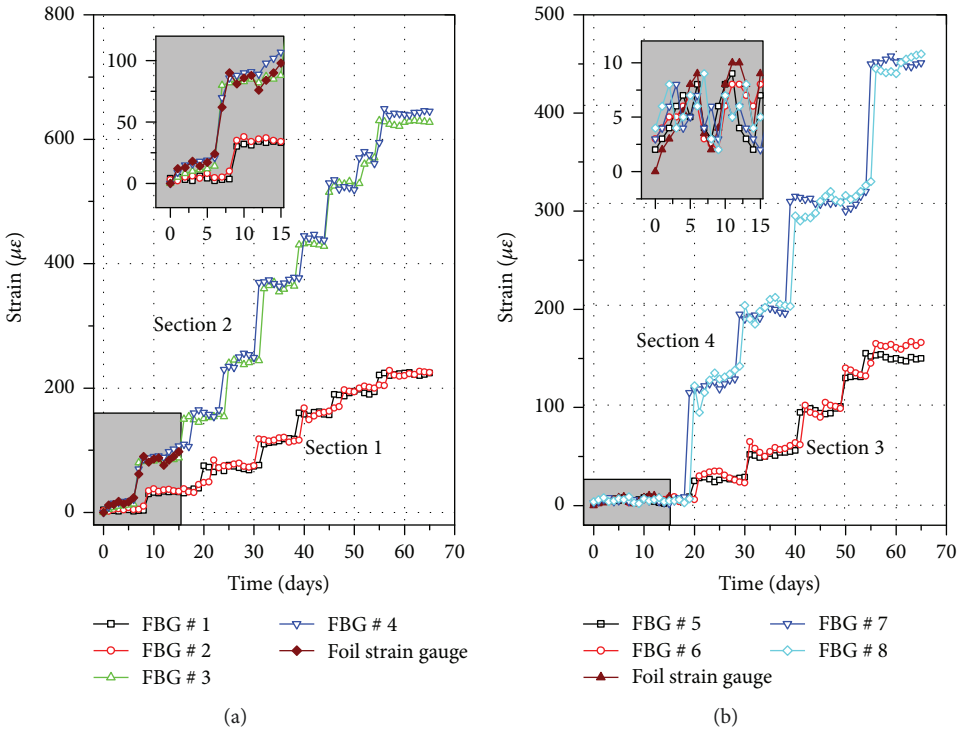

Figure 8: (a) Strain variations of FBG strain sensors at sections 1 and 2. (b) Strain variations of FBG strain sensors at sections 3 and 4.

observation period, strain measurements began in July 2016. First, 2100 distinct strain measurements (175 from each sensor) were recorded to define the stiffness matrix for the healthy mine state; these readings were also helpful for introducing artificial intelligence at later stages. The PCA compressed readings were sensitive enough to represent minute structural changes without losing any useful information.

4.3. Experimentation. Few experiments were performed in the mine to determine the DIM under different operating conditions and dynamic operation of the mine. During experimentation, extra precautions were taken to ensure the miners' working and personal safety. First, the stiffness matrix for the healthy mine state was determined as a baseline. Then, experiments were performed that were related to stiffness matrix reduction. For stiffness reduction, artificial damages were induced in the system by displacing or completely removing wooden mine supports (Figure 9(a)). To observe the maximum effect of disturbances in stiffness reduction, disturbances were created in the vicinity of the installed FBG strain monitoring station by removing wooden mine supports and leaving the span unsupported. The sequence of disturbances for each state is shown in Figure 9(b). For experimentation, section 1 (main roadway of mine) was selected for wooden support removal. The intact or healthy mine state baseline was denoted as state # 1. The damage scenarios were state # 2, state # 3, state # 4, and state # 5, with a stiffness reduction of 2%, 5%, 10%, and 15%, respectively.

4.4. Data Acquisition. In this study, the client was provided with real-time monitoring and data analysis in the form of a Web 2.0 page. The application process can be divided into three distinct steps. The first step involves real-time data acquisition, filtering, denoising, and filtered data acquisition. For this purpose, we utilized an RODB to handle the large amount of data. The second step is data aggregation to produce the structural statistics and strain matrix, which are based on the median and quartiles of the strain datasets. For this purpose, the proposed system utilized ETL for handling instantaneous inquiries of users followed by OLAP. The final output for the user can be stored in the database and also sent to CoAP [45]. CoAP is an IETF-proposed standard suitable for machine-to-machine or IoT interactions. The design of CoAP is similar to Hypertext Transfer Protocol (HTTP) with a smaller subset of Representational State Transfer (REST). CoAP uses the same method as HTTP for sending requests from the user to the client server, for example, GET, PUT, POST, and DELETE. Because of the smaller amount of overheads and easy fulfillment of the required system, CoAP was used as the application gateway [46].

5. Results

5.1. Online Condition Monitoring. CoAP was used in this study because of its simplicity and easy integration of web services for the generation of HTTP. Convergence of various standards, components, and applications is critical to the IoT. An application programming interface (API) was created using REST. This real-time safety and early-warning system also utilized a service-oriented approach (SOA) architecture for simplification and organized data orientation. A novel system of early warnings using Web 2.0 was generated by integrating and developing synergy between the different

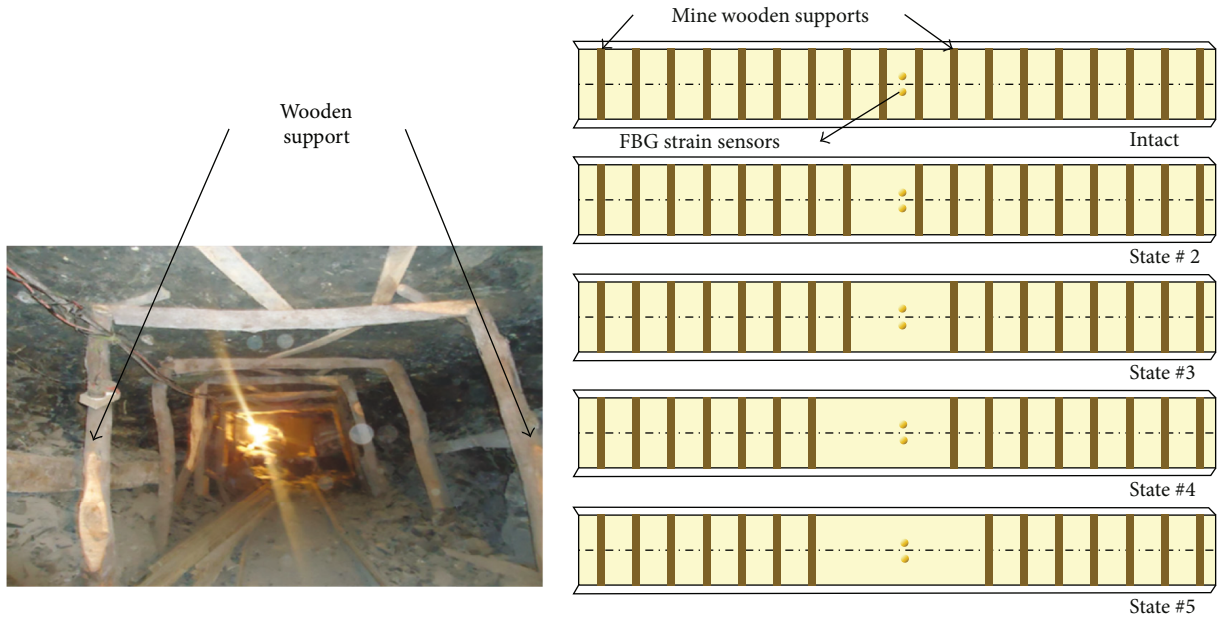

Figure 9: (a) Mine opening with installed wooden supports. (b) Sequence for the removal of mine wooden support during experimentation.

internet protocols (Figure 10). The work of Web 2.0 can be distinguished by two functions: (i) background operation that collects data and analyzes it and (ii) data representation that allows dynamic representation.

Figure 8 shows the tensional strain of all FBG strain sensors after necessary temperature compensation. This study focused on monitoring the mine roadway and access galleries because of the long-term stability required of these elements, as stability is negatively affected by continuous coal excavation. Figure 8(a) shows the strain variations for FBG strain sensors 1 and 2 (section 1) compared to sensors 3 and 4 (section 2). All of these FBG strain values vary with the face advance and distance of the production face. At the end of monitoring, the strain variations in section 1 leveled off at 260 $\mu\varepsilon$, while the highest values for section 2 were approximately 650 $\mu\varepsilon$. The strain values obtained from section 1 were 65% lower than those from section 2. This can be attributed to the good support installation in the main mine roadway compared to the access galleries, as the main haulage way should remain open and undisturbed for the entire life of the mine. Section 2 is also closer to the mine excavation face, resulting in a high amount of strain. As the production face comes closer to sections 1 and 2, there is an increasing overall trend in strain variations. However, until the end of the monitoring period (65 days), the strain values at both sections 1 and 2 were within the acceptable range.

Figure 8(b) shows the strain variations of sections 3 and 4 installed with strain sensors 5, 6 and 7, 8, respectively. The strain variations of FBG sensors 5 and 6 (mine roadway) gradually increased to 150 $\mu\varepsilon$, while the strain variations of section 4 increased to 450 $\mu\varepsilon$. The strain variations of section 4 were 68% higher than those of section 3 due to the wooden steel support installation in the main mine roadway. When we compare the strain variations of section 1 (roadway) and section 3 (roadway), section 1 variations were 43% higher than those of section 3. This is attributed to the shaft located near section 1. Moreover, at the time of development for the section 1 mine roadway, there was significantly less knowledge of the surrounding rock nature. However, at the time of excavation and support installation, by carefully considering the rock nature and mine opening characteristics, rock support was selected. The strain variations at section 4 were 38% lower compared to those of section 2, which can be better explained by the shorter opening width in section 4.

5.2. Data Fusion and Clustering Results. Determination of the PCs in PCA is of prime importance for singular value decomposition as was applied to the strain sensor readings, which provided the eigenvalues and their respective variance percentages. Figure 11 clearly indicates that the first two PCs cover more than 99% of the variance characterization of the available strain measurements. The insignificant contribution of the remaining PCs allows them to be ignored. Thus, the first two PCs were retained while the others were ignored. These retained PCs are helpful to project the original data onto the PC space domain. In this projection, new coordinates are chosen for which the original data contains the most variance.

In the hierarchical cluster analysis of the mine strain sensors, the bottom up approach was implemented to merge clusters with a similar structure. This study considers an unsupervised hierarchical cluster by implementing the average linkage method to detect clusters in the data, for which the confined distance matrix acts as an input. The results are presented in a dendrogram (Figure 12). In this hierarchical clustering, the x-axis presents the number of objects considered, which is eight in this case. The y-axis of the dendrogram represents the dissimilarity or distance between the clusters. This dendrogram represents the DIM comprised of four clades of eight leaves, two clusters, and one link by

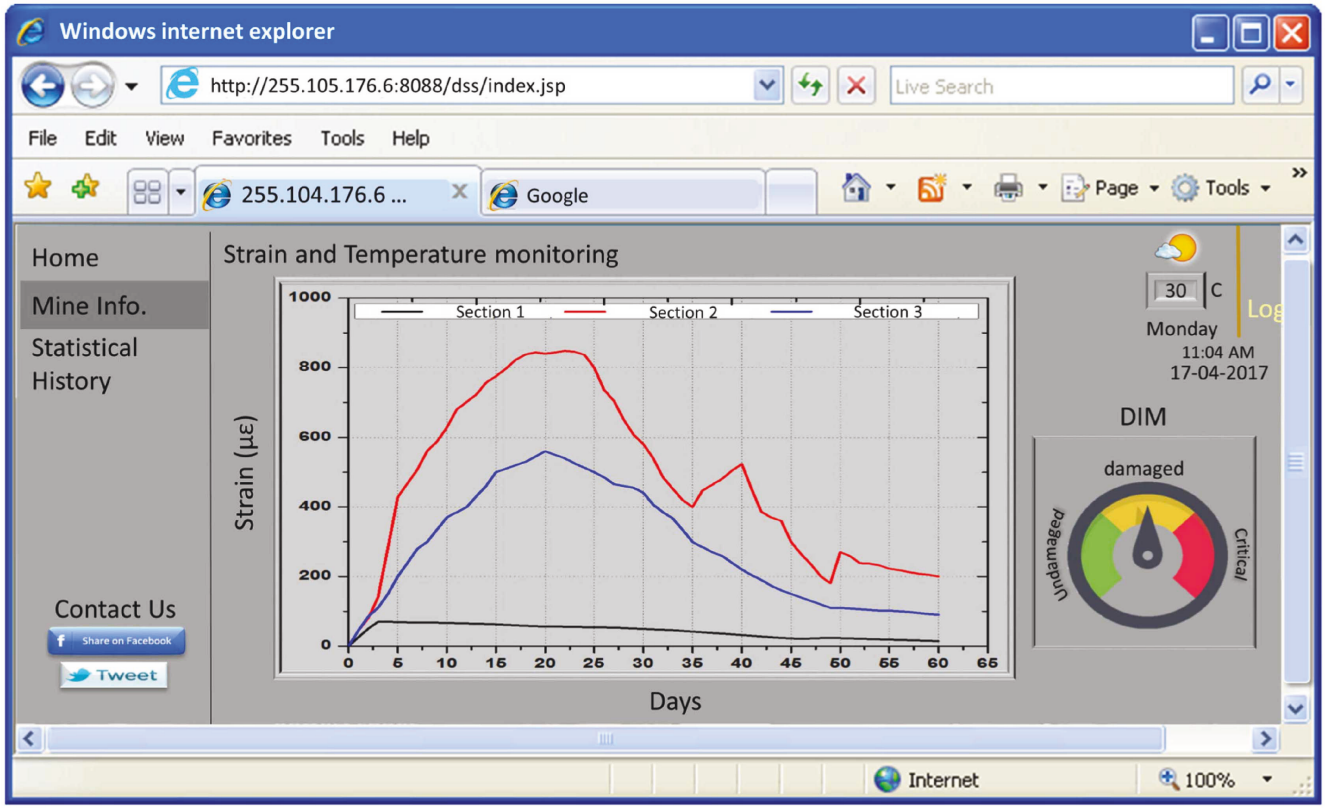

Figure 10: Web page screen shot of the proposed IoT-structural health monitoring platform for underground coal mines.

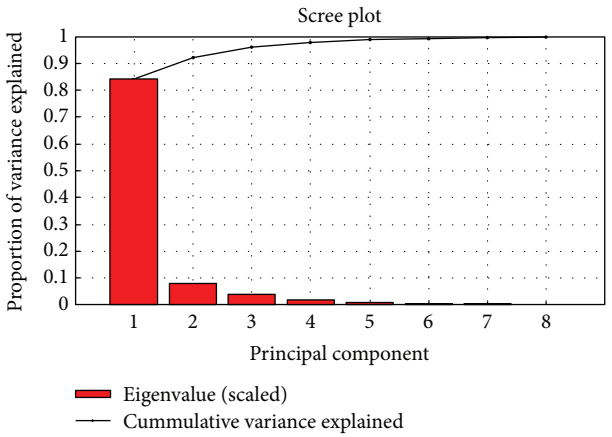

Figure 11: Normalized eigenvalues and variance of estimated sets.

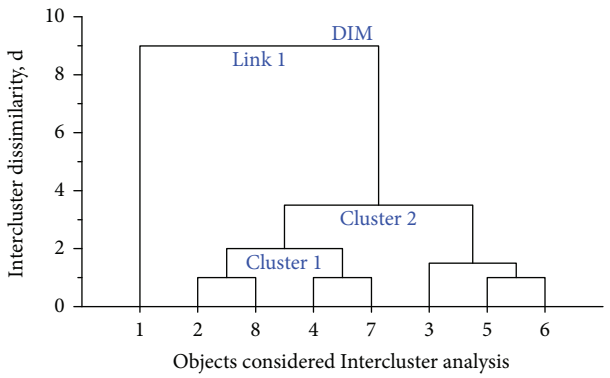

Figure 12: Dendrogram plot of hierarchical clustering, which merges eight data points using the bottom up approach. The merging process is such that the most similar objects will merge the first and higher levels containing one less object, ultimately resulting in a single value.

following the bottom up approach. In this study, the dendrogram (Figure 12) was plotted for the healthy state of the underground mine. Cluster 2 with the highest value was fixed as the reference cluster, and the relative distances of the other clusters were always found to be greater than 1, representing a healthy mine state. Thus, the dendrogram enables quick assessment of the mine structure by detecting minute changes in the monitoring values.

Figure 13(a) illustrates the DIM calculated based on the Euclidean Ichino-Yaguchi and Mahalanobis distances by considering PC1. The x-axis shows the damage states, and the y-axis represents the DIM value. State # 1 corresponds to the intact state; therefore, the DIM of this state starts at zero. For the successive damage states, DIM was plotted in the same figure, clearly indicating the differences between the damage scenarios (state # 2–state # 5) and the intact condition (state # 1). Figure 13(b) was plotted between the damage state values and DIM considering PC2. Both of these figures clearly separate the damage and healthy states, thus, successfully detecting all damages. The DIM in the case of

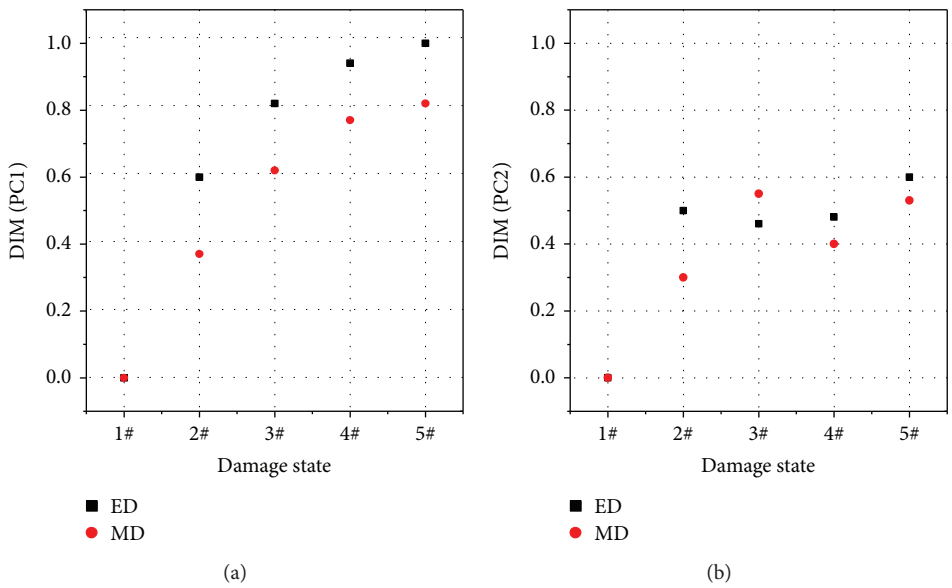

Figure 13: Damage index of the mine (DIM) for the selected PCs: (a) PC1 and (b) PC2.

PC2 varies, and the differences with the Euclidean and Mahalanobis distances are relatively smaller, which are attributed to the greater contribution of PC1 to the total variance of the system. However, despite accurate damage detection, it is difficult to quantify damages. Hence, further studies are needed for the quantification of damages.

The $\mathrm{DIM}_{(m)}$ of the selected PCs calculated using (18) is illustrated in Figure 14. All damage scenarios (state # 2 to state # 5) are clearly separated from the baseline (intact state). Given that PC1 contributes more than PC2 in the total variance of the system, a better performance for PC1 is observed. Consequently, it can be said that all damages have been successfully detected. For damage quantification, more investigations are needed to compare the DIM and $\mathrm{DIM}_{(m)}$ performances under varying and similar operating mine conditions.

Figure 15 shows the $N_{(z)}$ of the selected PCs for state # 1 and the damage scenarios. In this case, the first and last damages (2% reduction and 15% reduction, resp.) were successfully detected. For the other damages (state # 2 and state # 3), damages are vague and offer challenges to draw a conclusion, as the $N_{(z)}$ values are very small (0.2 and 0.3, resp.). On the contrary, the $N_{(z)}$ values greater than 0.45 provided more confidence for damage detection. By comparing Figures 13(a) and 13(b) with Figure 15, it can be concluded that the $N_{(z)}$ index is less accurate compared to the proposed indicator (DIM).

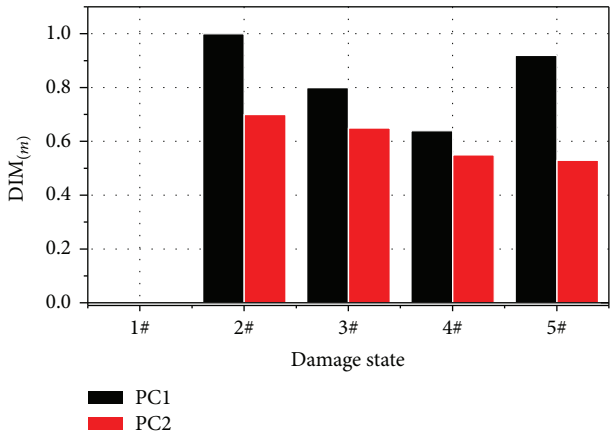

Figure 14: Damage indicator of the mine using the Mahalanobis distance (DIM_m) of PC1 and PC2 for state # 1 to state # 5.

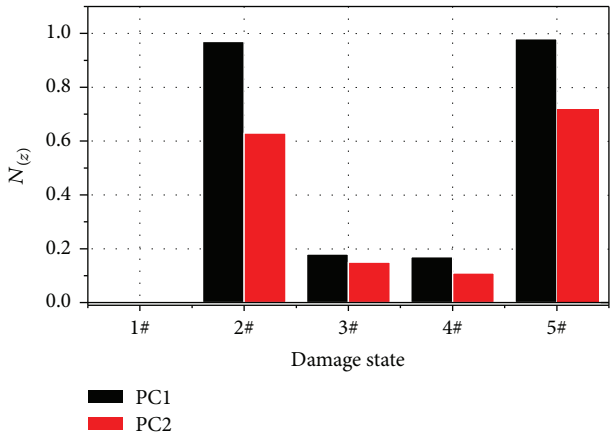

Figure 15: $N_{(z)}$ of PC1 and PC2 for state # 1 to state # 5.

6. Conclusion

This study introduced an IoT-based real-time monitoring, data-driven strategy for damage detection and a remote information sharing platform using quasi-distributed FBG sensors to enhance the structural safety of underground mines. This data-driven strategy fuses monitored datasets into a single-valued index without complex computation.

Furthermore, real-time perception, transmission, data-driven models, and application layers for the IoT-based UCM safety system were designed, developed, and validated in a real situation. The proposed system was successfully implemented at the operating Hassan Kishore coal mine in the Salt Range region of Punjab Pakistan. The results demonstrated that FBG sensors can reliably and continuously monitor the effects of dynamic mining activities on the structural stability of mines. The comparison of strain variations at mine roadway and access gallery demonstrated that the strain at the access galleries was higher. PCA can effectively reduce the mine monitoring data without losing imperative information, while clustering analysis is supportive of defining a mine damage index with high sensitivity to represent minute structural changes. Therefore, the proposed strategy of data analysis is sensitive to early damages. In addition, this system is capable of efficiently providing SHM data anytime and anywhere over the Internet. Therefore, this system is highly appropriate for shifting the reactive approaches of mine structural monitoring to proactive damage detection and accident prevention strategies. Thus, this IoT platform should be adopted for the structural safety of underground mines of high economic value to save miners' lives. One limitation is that the harsh conditions of underground mines may hamper the normal implementation of technologies and tools.

Conflicts of Interest

The authors declare that there is no conflict of interest regarding the publication of this paper.

Authors' Contributions

ByungWan Jo conceived the idea and provided the materials and technical support. Rana Muhammad Asad Khan carried out the implementation, data collection, and management and conducted different analyses on the related data. Yun Sung Lee, Jun Ho Jo, and Nadia Saleem helped in writing this paper.

Acknowledgments

The authors would like to thank the anonymous reviewers for their constructive comments and suggestions on improving this paper.

References

[1] J. M. Patterson and S. A. Shappell, "Operator error and system deficiencies: analysis of 508 mining incidents and accidents from Queensland, Australia using HFACS," *Accident Analysis & Prevention*, vol. 42, no. 4, pp. 1379–1385, 2010.

[2] W. Cai, L. Dou, A. Cao, S. Gong, and Z. Li, "Application of seismic velocity tomography in underground coal mines: a case study of Yima mining area, Henan, China," *Journal of Applied Geophysics*, vol. 109, pp. 140–149, 2014.

[3] LLP, AI, "Causes of mining and cave-in accidents," [cited 2017], https://www.industrialinjuryattorney.com/Industrial-Accident-Blog/2014/July/Causes-of-Mining-and-Cave-in-Accidents.aspx.

[4] E. Saddique, "Annual report, 2011 of chief inspectorate of mines, Punjab," [cited April 2017] 2011, https://cim.punjab.gov.pk/system/files/CIM_AnnualReport_2011.pdf.

[5] L.-m. Dou, Z.l. Mu, Z.l. Li, A.y. Cao, and S.y. Gong, "Research progress of monitoring, forecasting, and prevention of rockburst in underground coal mining in China," *International Journal of Coal Science & Technology*, vol. 1, no. 3, pp. 278–288, 2014.

[6] M. Huang, Z. Zhou, Y. Huang, and J. Ou, "A distributed self-sensing FRP anchor rod with built-in optical fiber sensor," *Measurement*, vol. 46, no. 4, pp. 1363–1370, 2013.

[7] D. Kinet, K. Chah, A. Gusarov et al., "Proof of concept for temperature and strain measurements with fiber Bragg gratings embedded in supercontainers designed for nuclear waste storage," *IEEE Transactions on Nuclear Science*, vol. 63, no. 3, pp. 1955–1962, 2016.

[8] M. Debliquy, D. Lahem, A. Bueno-Martinez, G. Ravet, J.-M. Renoirt, and C. Caucheteur, "Review of the use of the optical fibers for safety applications in tunnels and car parks: pollution monitoring, fire and explosive gas detection," in *Sensing Technology: Current Status and Future Trends III*, pp. 1–24, Springer, Cham, 2015.

[9] Z. Zhou, Z. Wang, and L. Shao, "Fiber-reinforced polymer-packaged optical fiber Bragg grating strain sensors for infrastructures under harsh environment," *Journal of Sensors*, vol. 2016, Article ID 3953750, 18 pages, 2016.

[10] H. Naruse, H. Uehara, T. Deguchi et al., "Application of a distributed fibre optic strain sensing system to monitoring changes in the state of an underground mine," *Measurement Science and Technology*, vol. 18, no. 10, pp. 3202–3210, 2007.

[11] Y. Zhao, Z.-Q. Li, and Y. Dong, "Design and experiments on a wide range fiber Bragg grating sensor for health monitoring of coal mines," *Optik - International Journal for Light and Electron Optics*, vol. 125, no. 20, pp. 6287–6290, 2014.

[12] A. Klar, I. Dromy, and R. Linker, "Monitoring tunneling induced ground displacements using distributed fiber-optic sensing," *Tunnelling and Underground Space Technology*, vol. 40, pp. 141–150, 2014.

[13] C. Y. Gue, M. Wilcock, M. M. Alhaddad, M. Z. E. B. Elshafie, K. Soga, and R. J. Mair, "The monitoring of an existing cast iron tunnel with distributed fibre optic sensing (DFOS)," *Journal of Civil Structural Health Monitoring*, vol. 5, no. 5, pp. 573–586, 2015.

[14] B. Madjdabadi, B. Valley, M. B. Dusseault, and P. K. Kaiser, "Experimental evaluation of a distributed Brillouin sensing system for measuring extensional and shear deformation in rock," *Measurement*, vol. 77, pp. 54–66, 2016.

[15] H.-F. Pei, J. Teng, J. H. Yin, and R. Chen, "A review of previous studies on the applications of optical fiber sensors in geotechnical health monitoring," *Measurement*, vol. 58, pp. 207–214, 2014.

[16] W. He, G. Yan, and L. Da Xu, "Developing vehicular data cloud services in the IoT environment," *IEEE Transactions on Industrial Informatics*, vol. 10, no. 2, pp. 1587–1595, 2014.

[17] E. Sun, X. Zhang, and Z. Li, "The internet of things (IOT) and cloud computing (CC) based tailings dam monitoring and pre-alarm system in mines," *Safety Science*, vol. 50, no. 4, pp. 811–815, 2012.

[18] S. Fang, L. Da Xu, Y. Zhu et al., "An integrated system for regional environmental monitoring and management based

on internet of things," *IEEE Transactions on Industrial Informatics*, vol. 10, no. 2, pp. 1596–1605, 2014.

[19] P. Ferdinand, S. Magne, V. Dewynter-Marty, C. Martinez, S. Rougeault, and M. Bugaud, "Applications of Bragg grating sensors in Europe," in *12th International Conference on Optical Fiber Sensors*, pp. 14–19, Williamsburg, VA, USA, 1997, Optical Society of America.

[20] M. Majumder, T. K. Gangopadhyay, A. K. Chakraborty, K. Dasgupta, and D. K. Bhattacharya, "Fibre Bragg gratings in structural health monitoring—present status and applications," *Sensors and Actuators A: Physical*, vol. 147, no. 1, pp. 150–164, 2008.

[21] C.-Y. Hong, Y. F. Zhang, M. X. Zhang, L. M. G. Leung, and L. Q. Liu, "Application of FBG sensors for geotechnical health monitoring, a review of sensor design, implementation methods and packaging techniques," *Sensors and Actuators A: Physical*, vol. 244, pp. 184–197, 2016.

[22] F. Xie, S. Zhang, Y. Li, and S. B. Lee, "Temperature-compensating multiple fiber Bragg grating strain sensors with a metrological grating," *Optics and Lasers in Engineering*, vol. 41, no. 1, pp. 205–216, 2004.

[23] M. Botts, G. Percivall, C. Reed, and J. Davidson, "OGC® sensor web enablement: overview and high level architecture," in *GeoSensor Networks*pp. 175–190, Springer, Berlin, Heidelberg.

[24] G. Luyckx, E. Voet, N. Lammens, and J. Degrieck, "Strain measurements of composite laminates with embedded fibre Bragg gratings: criticism and opportunities for research," *Sensors*, vol. 11, no. 1, pp. 384–408, 2011.

[25] Micron Optics, "Os3610," [cited 2017], http://www.micronoptics.com/product/surface-mount-strain-sensor-os3610/.

[26] Micron Optics[cited 2017], http://www.micronoptics.com/wp-content/uploads/2017/07/os4300-2.pdf.

[27] M. J. Kim, Y. H. Kim, G. Mudhana, and B. H. Lee, "Simultaneous measurement of temperature and strain based on double cladding fiber interferometer assisted by fiber grating pair," *IEEE Photonics Technology Letters*, vol. 20, no. 15, pp. 1290–1292, 2008.

[28] M. Xu, J. L. Archambault, L. Reekie, and J. P. Dakin, "Thermally-compensated bending gauge using surface-mounted fibre gratings," *International Journal of Optoelectronics*, vol. 9, no. 3, pp. 281–284, 1994.

[29] Corning, "SMF-28," [cited 2017], http://ece466.groups.et.byu.net/notes/smf28.pdf.

[30] Micron Optics Inc, "sm 125 optical interogator," [cited January 2017], http://www.micronoptics.com/.

[31] X. G. Hua, Y. Q. Ni, Z. Q. Chen, and J. M. Ko, "Structural damage detection of cable-stayed bridges using changes in cable forces and model updating," *Journal of Structural Engineering*, vol. 135, no. 9, pp. 1093–1106, 2009.

[32] V. Meruane and W. Heylen, "Structural damage assessment under varying temperature conditions," *Structural Health Monitoring*, vol. 11, no. 3, pp. 345–357, 2012.

[33] D. Posenato, P. Kripakaran, D. Inaudi, and I. F. C. Smith, "Methodologies for model-free data interpretation of civil engineering structures," *Computers & Structures*, vol. 88, no. 7-8, pp. 467–482, 2010.

[34] K. N. Kesavan and A. S. Kiremidjian, "A wavelet-based damage diagnosis algorithm using principal component analysis," *Structural Control & Health Monitoring*, vol. 19, no. 8, pp. 672–685, 2012.

[35] O. R. de Lautour and P. Omenzetter, "Damage classification and estimation in experimental structures using time series analysis and pattern recognition," *Mechanical Systems and Signal Processing*, vol. 24, no. 5, pp. 1556–1569, 2010.

[36] S. Wold, K. Esbensen, and P. Geladi, "Principal component analysis," *Chemometrics and Intelligent Laboratory Systems*, vol. 2, no. 1-3, pp. 37–52, 1987.

[37] H. Abdi and L. J. Williams, "Principal component analysis," *Wiley Interdisciplinary Reviews: Computational Statistics*, vol. 2, no. 4, pp. 433–459, 2010.

[38] J. A. Westerhuis, T. Kourti, and J. F. MacGregor, "Comparing alternative approaches for multivariate statistical analysis of batch process data," *Journal of Chemometrics*, vol. 13, no. 3-4, pp. 397–413, 1999.

[39] Y. L. Zhou, E. Figueiredo, N. Maia, R. Sampaio, and R. Perera, "Damage detection in structures using a transmissibility-based Mahalanobis distance," *Structural Control & Health Monitoring*, vol. 22, no. 10, pp. 1209–1222, 2015.

[40] A. Cury, C. Crémona, and E. Diday, "Application of symbolic data analysis for structural modification assessment," *Engineering Structures*, vol. 32, no. 3, pp. 762–775, 2010.

[41] J. Santos, *Smart Structural Health Monitoring Techniques for Novelty Identification in Civil Engineering Structures, [Ph.D. Thesis]*, Instituto Superior Técnico–University of Lisbon, Lisbon, Portugal, 2014.

[42] Z. John Lu, "The elements of statistical learning: data mining, inference, and prediction," *Journal of the Royal Statistical Society: Series A (Statistics in Society)*, vol. 173, no. 3, pp. 693-694, 2010.

[43] J. P. Santos, C. Crémona, A. D. Orcesi, and P. Silveira, "Multivariate statistical analysis for early damage detection," *Engineering Structures*, vol. 56, pp. 273–285, 2013.

[44] K. Worden, G. Manson, and D. Allman, "Experimental validation of a structural health monitoring methodology: part I. Novelty detection on a laboratory structure," *Journal of Sound and Vibration*, vol. 259, no. 2, pp. 323–343, 2003.

[45] Z. Shelby, K. Hartke, and C. Bormann, "Constrained application protocol (CoAP)," vol. 1, 2014.

[46] C. Bormann, A. P. Castellani, and Z. Shelby, "Coap: an application protocol for billions of tiny internet nodes," *IEEE Internet Computing*, vol. 16, no. 2, pp. 62–67, 2012.